



HAL
open science

Low-energy electron control over physical and chemical properties of organic aromatic thin layers at the micrometre scale

Qiang Wu, Leo Sala, Lionel Amiaud, Claire Mathieu, Christophe Lubin, Anne Lafosse, Nick Barrett

► To cite this version:

Qiang Wu, Leo Sala, Lionel Amiaud, Claire Mathieu, Christophe Lubin, et al.. Low-energy electron control over physical and chemical properties of organic aromatic thin layers at the micrometre scale. 2021. hal-03207966

HAL Id: hal-03207966

<https://hal.science/hal-03207966>

Preprint submitted on 26 Apr 2021

HAL is a multi-disciplinary open access archive for the deposit and dissemination of scientific research documents, whether they are published or not. The documents may come from teaching and research institutions in France or abroad, or from public or private research centers.

L'archive ouverte pluridisciplinaire **HAL**, est destinée au dépôt et à la diffusion de documents scientifiques de niveau recherche, publiés ou non, émanant des établissements d'enseignement et de recherche français ou étrangers, des laboratoires publics ou privés.

Low-energy electron control over physical and chemical properties of organic aromatic thin layers at the micrometre scale

Qiang Wu^{1,2}, Leo Sala¹, Lionel Amiaud^{1*}, Claire Mathieu², Christophe Lubin², Anne Lafosse¹, Nick Barrett²

¹Université Paris-Saclay, CNRS, Institut des Sciences Moléculaires d'Orsay, 91405, Orsay, France and ²SPCS, CEA, CNRS, Université Paris-Saclay, CEA Saclay, 91191 Gif-sur-Yvette Cedex, France.

* Corresponding author Email: lionel.amiaud@u-psud.fr

Abstract

The collimated monochromatic low-energy (≤ 50 eV) electron beam delivered by a low energy electron microscope (LEEM) was used to locally modify organic molecular thin films at the micrometre-scale. Self-Assembled Monolayers (SAMs) of p-terphenylthiol (TPT) anchored on gold substrates were used as model organic layers. The local work function (WF) was observed to decrease as a consequence of electron irradiation and to be tuneable using the irradiation energy and/or the dose as control parameters. The chemical origin of the observed WF changes could be discussed in the light of available vibrational analyses of irradiated TPT SAMs performed using High-Resolution Electron Energy Loss Spectroscopy (HREELS) and by comparing the effective cross sections estimated for WF modulation and for chemical modifications, respectively. The hydrogen content of the organic thin film was shown to be the determining parameter, rather than the degree of aromaticity of the hydrogenated carbon centres. Finally, the imprinted modifications were observed to have a moderate stability after air exposure by combining Photoemission Electron Microscopy (PEEM) and HREELS.

Keywords - Low energy electron irradiation; chemical modification; LEEM; HREELS; work function tuning; SAM.

Introduction

To pattern templates of controlled chemical composition with a high spatial resolution is a prerequisite in the development of sensing platforms [1–5]. One method to tune locally the physical and chemical properties of an organic-inorganic hybrid system is to process thin molecular layers serving as platforms for device development using photons or electrons. State of the art chemical template goes down to scale of few tens of nanometers [5–7], but there are also interest for micrometre scale molecular architectures, for example when it comes to objects of biological interest like viruses and designed proteins [8–10].

High energy irradiations are used to reach high spatial resolution, but provide less control over specific chemical modifications. Many reactivity channels are open and competing at these energies, among which processes triggered by secondary low-energy electrons (LEE, ≤ 50 eV) are contributing. LEE are known as efficient particles to induce selective chemical modifications [11,12], and thereby associated physical property modifications [13]. Highly focussed LEE beams are difficult to produce, mainly due to space charge. But a way to go down in terms of beam diameter is to process molecular layers using a collimated beam delivered by a LEEM. Therefore LEEM experiments were performed to locally modify the molecular layer and image the local modification of the physical properties of the organic thin films. The related induced chemical modifications were investigated using vibrational spectroscopy after layer processing at the same energies using a standard electron gun delivering centimetre scale beam.

Self-assembled monolayers (SAMs) are ordered assemblies of densely packed organic molecules chemisorbed on inorganic substrates. In recent years, SAMs have been widely used in nanotechnology due to the flexibility offered by the chemical composition adaptability [14,15]. Aromatic SAMs exhibit a negative resist behaviour due to their cross-linking ability, the reticulation proceeding through the creation of bonds between neighbour molecules in the layer [16]. Crosslinked aromatic SAMs were indeed used to build molecular devices, containing robust anchors and templates for biomolecules, or used as good precursors for producing carbon nanosheets and nanomembranes [8,16–18]. Aromatic SAMs of *p*-terphenylthiol (TPT) are good candidates to demonstrate the feasibility of using low-energy electron processing to control physical and chemical properties of organic aromatic thin layers at the micrometre scale.

In this work, we demonstrate that chemical modifications can be induced on a microscopic scale through the use of a LEEM [19], providing a possible efficient alternative to less selective high energy electron irradiation. In order to correlate the electronic structure changes with chemical modifications induced by low energy electron irradiations to the TPT films, the WF of the irradiated TPT film was measured by both LEEM and photoemission electron microscopy (PEEM). The WF decreases by up to 0.27 eV in TPT films following irradiation energies from 10 to 50 eV. However, the irradiation with electron energy of 6 eV, known to induce the carbon hybridization state transition from sp^2 to sp^3 in TPT SAMs [20], does not bring detectable WF change. Besides, the position of the higher occupied molecular orbital (HOMO) of TPT SAMs does not change with respect to Fermi level after irradiation. The WF is then confronted to chemical modification in an attempt to interpret which chemical characteristics are decisive in setting the WF of a supported organic aromatic layer.

Commenté [LS1]: This was true for all energies we tried (?)

Results and discussion

SAMs of TPT molecules (1,1',4',1''-Terphenyl-4-thiol HS-(C₆H₄)₂-C₆H₅) supported on gold layers, as schematized in Fig. 1, are good model layers to study physical & chemical modifications induced under electron irradiation at the sub-micrometre scale. These molecular platforms belong to a family of organic aromatic layers already implemented as resist films for chemical lithography and development of molecular devices and membranes [8,21,22]. These molecular films are dense ($\sim 4.6 \times 10^{14}$ molecules.cm⁻²) [23], 2D-organized and conductive enough to prevent charge accumulation during low-energy electron irradiation. Their thickness of about 15 Å [24,25] is shorter than the irradiation depth of 3 times the mean free path, estimated in the range 7-12 Å - [26–28]. Their thickness is furthermore smaller than the HREELS probing depth, which was evaluated to be 24-36 Å at $E_{\text{HREELS}} = 6$ eV in a previous study [29–31], so that the TPT SAMs are irradiated and probed vibrationally over their whole thickness.

Morphology of the aromatic SAMs deposited on gold substrate

The quality of the supporting Au coated layer is examined after flame-annealing by both atomic force microscope AFM (Fig. 1(a)) and LEEM (Fig. 1(b)). The expected crystalline micron-scale domains in the Au layer are clearly observed. A careful

procedure is followed for the TPT SAM preparation and spectroscopic characterization using HREELS (see experimental section and below). The micro-scale domains are again clearly observed in the LEEM images of the supported TPT SAMs (see Fig. 2). The μ -LEED taken in different areas with a 2 μm electron beam in LEEM shows the FCC(111) preferential orientation of the TPT SAM domains, with different azimuthal (in-plane) orientations (Fig. 1(c) and (d)), as expected from the textured polycrystalline Au topmost layers [32,33].

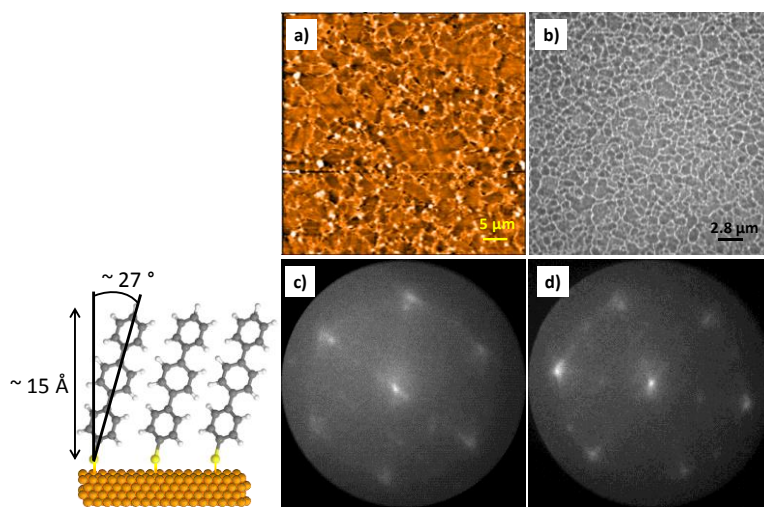


Figure 1: Crystalline micron-scale domains of the flame-annealed polycrystalline Au layer are clearly observed, both by AFM (a) and LEEM taken at incident energy 0.3 eV (b). In (c) and (d), μ -LEED patterns produced by LEEM with a 2 μm electron beam at different areas on TPT/Au sample show azimuthal rotation of lattice.

Spot imprinting using LEEM beam

The primary irradiations using the LEEM beam were done with electron energies selected according to previous studies performed using a standard electron gun delivering a centimetre-scale beam [31,34,35]. A pristine TPT SAM was irradiated on different spots at 1 eV, 6 eV, 10 eV, 20 eV, 30 eV, 40 eV, and 50 eV using the same electron dose estimated at about 95 $\text{mC}\cdot\text{cm}^{-2}$. LEEM images presented in Fig. 2(a) and 2(b) are recorded immediately after the imprinting of the spots. When visible, the irradiation footprint is precisely confined with sharp edges corresponding to the 5 μm collimated beam of slightly elliptical shape. Compared to the non-irradiated

surroundings, the area irradiated at 50 eV shows strong contrast which gradually weakens when going down in energy. On the other hand, the areas irradiated by 6 eV and 1 eV electrons do not show any clear contrast with the surrounding (non-irradiated) area.

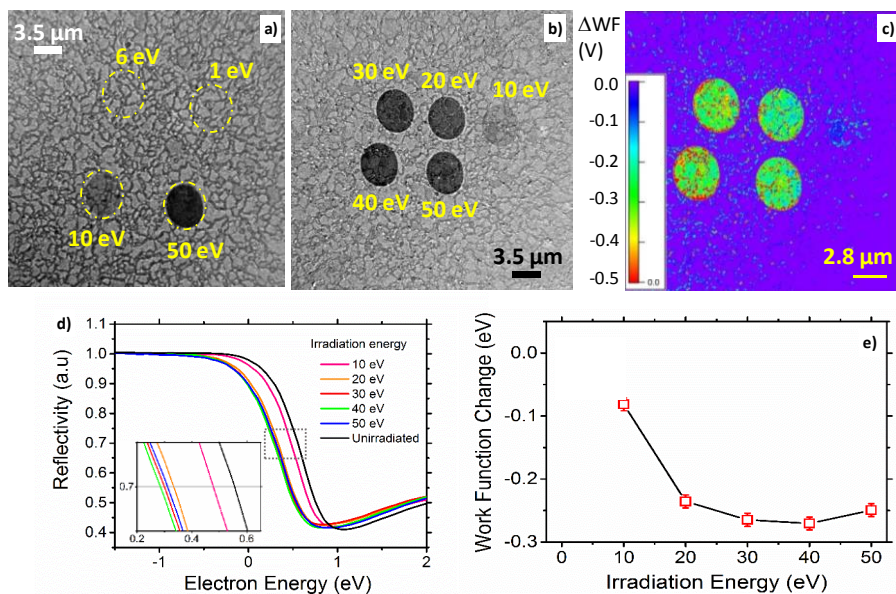


Figure 2: LEEM images ((a) and (b), taken at start voltages of 0.6 eV and 0.3 eV, respectively) of TPT SAMs supported on gold irradiated with different energies (indicated in the image) on separated 5 μm spots (dose: 95 mC.cm⁻²). The irradiated areas are marked with dash-dot outlined circles. (c) Map of WF variations ΔWF deduced from the pixel-by-pixel analysis of the energy positions of the MEM-LEEM transition for the irradiation pattern shown in panel (b). (d) MEM-LEEM transition curves obtained by averaging over the areas irradiated with different energies. (e) Average work function variation with respect to the pristine film as a function of the irradiation energy.

The contrast is related to the modification of the sample electron reflectivity and work function. It can be rationalized by measuring the transition from mirror electron microscopy (MEM) mode to LEEM imaging mode [36,37] immediately after irradiation (see experimental section). The electron reflectivity curves are fitted with an error function to determine the energy positions of the MEM-LEEM transition [38], and the

obtained WF variations with respect to the unirradiated area (ΔWF) can be represented pixel-by-pixel by color contrast as in the position map of Fig. 2(c). The electron reflectivity curves presented in Fig. 2(d) are obtained by averaging over each irradiation spot. The deduced average WF changes are represented as a function of the irradiation electron energy in Fig. 2(e). No appreciable WF change of TPT SAMs can be observed for the lower irradiation energies. The WF decreases notably by 0.08 eV after irradiation at 10 eV, before reaching a negative plateau around 0.25-0.27 eV over the range 20-50 eV for a fixed dose 95 mC.cm⁻².

Cross-section estimation for WF change induced by irradiation at 10 and 50 eV

The effect of irradiation dose on the WF changes induced in TPT SAMs is examined by comparing the average MEM-LEEM transition positions for incremental irradiation time (in the 0-30 min range) with either 10 eV or 50 eV electrons. The experimental data points are plotted in Fig. 3. In both cases the work function decreases at increasing irradiation dose before reaching an asymptote. These irradiation-induced modifications are fitted by a standard exponential decay: $\Delta WF(d) = \Delta WF_{\infty}[1 - \exp(-\sigma d)]$, where d is the cumulated irradiation dose, ΔWF_{∞} is the asymptotic WF modification reached and σ the associated effective cross section. At 10 eV the WF decreases slowly in the considered dose range towards an asymptotic change of $\Delta WF_{\infty}(10 \text{ eV}) = -0.12 \text{ eV}$, with an associated cross section estimated at $\sigma(10 \text{ eV}) = 1.4 \times 10^{-18} \text{ cm}^2$. At 50 eV the WF decreases abruptly and reaches a significantly lower asymptotic value, corresponding to $\Delta WF_{\infty}(50 \text{ eV}) = -0.23 \text{ eV}$, with $\sigma(50 \text{ eV}) = 1.6 \times 10^{-17} \text{ cm}^2$. The work function of the sample can be tuned locally at the micrometre scale, over a limited range, using the irradiation energy and the delivered dose as control parameters. These measurements can also be regarded as an evaluation of the stability of the molecular films when submitted to electron fluxes. Once the saturation regime has been achieved, the WF of the molecular platform is stabilized and unaffected by further irradiation.

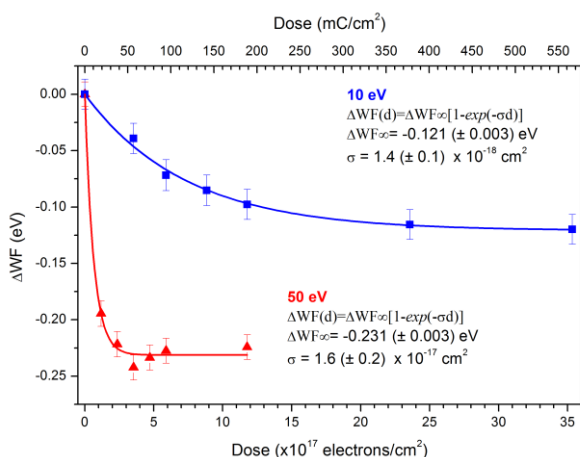


Figure 3: Work function changes (ΔWF) as a function of the irradiation dose (in electrons. cm^{-2} and in $\text{mC}.\text{cm}^{-2}$ for the lower and upper scales, respectively) for 10 eV (red triangles) and 50 eV (blue squares) irradiation energies. The curves represent the exponential fits used to estimate the effective cross-sections for WF tuning and the given uncertainties are directly the statistical ones.

Chemical origin(s) of WF changes induced at different energies

Electron induced chemical modifications of aromatic SAMs were quite intensively studied because there are promising molecular platforms for device design. We used electron energy loss vibrational spectroscopy in previous studies [31,34] for the chemical characterization of the TPT SAMs. Particular attention was paid to the evolution of the hydrogen content and the hybridization state (sp^m , $m = 2, 3$) of the associated carbon centers. The band attributed to overlapping contributions of the CH stretching modes $\nu(sp^m-\text{CH}_x)$ is a well-isolated band, observed in the range 340-410 meV ($2740-3305 \text{ cm}^{-1}$). It can be used as a marker for the hydrogen content of the film, since its intensity depends on the hydrogen atom quantity, and its position & structure depend on the hybridization state of the partner carbon atoms. The $\nu(sp^m-\text{CH}_x)$ band is shown for TPT SAMs before and after electron irradiation at increasing energy in Fig. 4. The pristine film is characterized by a well-defined peak at 378 meV, attributed to the stretching modes $\nu(sp^2-\text{CH})$ and reflecting the fact that the hydrogenated carbon centers are unsaturated ones. The observed chemical

modifications depend dramatically on the incident electron energy. At 1 eV, no chemical changes can be identified. At 6 eV, a strong modification of the CH stretching signature is observed. The 368 meV peak decreases in intensity, while a new contribution appears centered at 367 meV. This new contribution can be attributed to stretching modes of CH_x groups, in which the carbon center is no longer unsaturated, but is in the sp^3 hybridization state. This demonstrates that a noticeable part of the hydrogenated aromatic carbon centers was converted into saturated ones. The intensity of the whole band does not vary, meaning that the hydrogen content does not vary significantly. These observations were related to cross-linking within the spacer layer. At 10 eV even at higher dose, just like at 1 eV, no sensitive chemical changes can be identified by HREELS. At 50 eV, again a strong modification of the CH stretching signature is observed, but strikingly different than the one obtained at 6 eV. The band is decreasing in intensity, without changing its global shape. This means that the probed hydrogenated carbon centers are still unsaturated, sp^2 -hybridized, but that the hydrogen content of the film has strongly decreased.

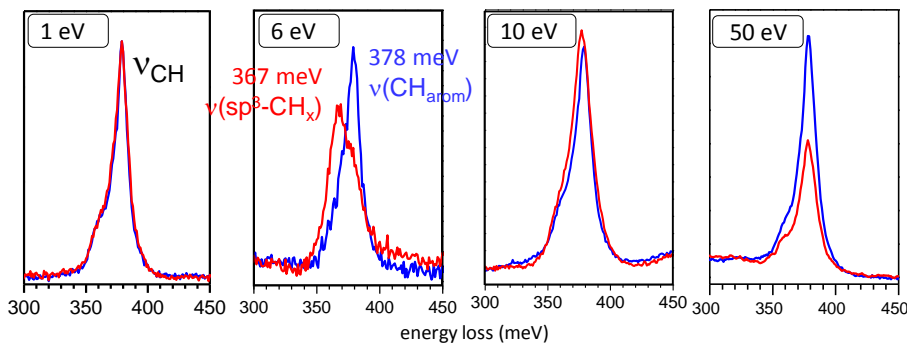


Figure 4: $\nu(sp^m\text{-CH}_x)$ band probed using vibrational spectroscopy ($E_{\text{HREELS}} = 6 \text{ eV}$, resolution $\Delta E_{\text{FWHM}} = 6\text{-}8 \text{ meV}$). Chemical modification of TPT SAMs submitted to electron irradiation at 1 eV (dose: $2.5 \text{ mC}\cdot\text{cm}^{-2}$), 6 eV (dose: $2.0 \text{ mC}\cdot\text{cm}^{-2}$), 10 eV (dose: $10.0 \text{ mC}\cdot\text{cm}^{-2}$) and 50 eV (dose: $3.4 \text{ mC}\cdot\text{cm}^{-2}$). The pristine film (blue spectrum) is characterized by a well-isolated $\nu(sp^m\text{-CH}_x)$ band at 378 meV, attributed to aromatic CH species ($sp^2\text{-CH}$). After irradiation (red spectra), the band is either not modified (1 eV), barely modified (10 eV), has a different structure but a constant area (6 eV), or still presents the same shape but with a reduced intensity (50 eV).

$E_{irr}(e^-)$	1 eV	6 eV	10 eV	50 eV
Dose (mC.cm ⁻²)	2.5	2.0	10.0	3.4
H Content	conserved	conserved	conserved	50 ± 5 %
sp ² -CH → sp ³ -CH	none	50 ± 5 %	none	< 5 %
Primary interaction		e ⁻ attachm ^t		ion. & exc
"chemical" σ_{eff} (cm ²)	/	~1.2×10 ⁻¹⁶	/	~2.7-4.7×10 ⁻¹⁷
"WF_modif" σ_{eff} (cm ²)	/	/	~1.4×10 ⁻¹⁸	~1.6×10 ⁻¹⁷

Table 1: Main induced chemical modifications, dominant electron-molecule primary interaction, the effective cross section associated to the chemical modification and the effective cross section for work function modification under electron impact are tabulated as a function of the irradiation energy.

We could further demonstrate that the electron attachment is the mechanism at work at 6 eV, and that the effective cross section associated to the hydrogenated carbon center re-hybridization is about $\sim 1.2 \times 10^{-16} \text{ cm}^2$ [34]. At 50 eV, both molecular electronic excitation and ionization under electron impact might contribute and the effective cross section resulting in the reduction of the hydrogen content is one order of magnitude smaller ($2.7\text{-}4.7 \times 10^{-17} \text{ cm}^2$) [31]. These quantitative data are listed in Table 1, together with the main primary mechanism at play and the nature of induced chemical modification. This emphasizes that the electron energy used for irradiation drives the nature of the induced chemical modifications. Under processing at 6 eV, the hydrogen content is preserved at the cost of a loss of aromaticity of the hydrogenated carbon centers. Under processing at 50 eV, the hydrogenated carbon centers remain unsaturated but a global hydrogen loss is undergone by the film. Since the TPT film thickness was demonstrated to remain unchanged under electron irradiation at 50 eV [39], a decrease in the hydrogen content is equivalent to an increase in the content of de-hydrogenated carbon centres, whose hybridization state cannot be easily probed. TPT SAM is partly converted into an amorphous carbon matrix. Note that additional chemical modifications of a related aromatic SAM, the biphenylthiol SAM (BPT), induced at 50 eV, were reported in the literature using IR and X-ray spectroscopies [40]. Hydrogen content decrease was observed also for this system using IR spectroscopy. It was interpreted as resulting in the production of a stabilized aromatic molecular layer through cross-linking [16,41,42]. Chemical induced disorder was deduced from C(1s) XPS signature with an associated cross-section of $3 \times 10^{-17} \text{ cm}^2$, a value comparable to the effective cross section derived above. It is also in the range

(i) of the structural disordering measured by near-edge X-ray absorption fine structure spectroscopy (NEXAFS) in BTP ($1.8 \times 10^{-17} \text{ cm}^2$), and (ii) of the alteration of the anchoring groups ($2.0 \times 10^{-17} \text{ cm}^2$) and their conversion into sulfide groups, R-S-R or R-SS-R ($1.5 \times 10^{-17} \text{ cm}^2$ [40,43] and $\sim 0.5 \times 10^{-17} \text{ cm}^2$ as estimated from Fig. 3 in ref. [44]). For TPT SAMs, carbon matrix and anchoring alteration cross section are respectively $3.7 (\pm 0.9) \times 10^{-17} \text{ cm}^2$ and $1.3 (\pm 0.3) \times 10^{-17} \text{ cm}^2$, under 10^{-8} mbar of H_2 pressure.

Some insights about the molecular origin of the WF changes can be gained by confronting the effect of the irradiation on the induced chemical modifications and the induced WF changes, as well as by comparing the estimated effective cross sections. The work function of a SAM differs from a clean Au(111) surface, as a combination of numerous contributions. An organic layer on a metal leads to a reduction of the surface dipole of the clean surface- a source of an attractive force for escaping electron. This so called "Pillow" effect reduces the extension of electron wave function in the vacuum, with a reduction of 0.1-0.2 eV of the work function[45]. In addition, energy differences between the metal Fermi level and the molecules HOMO and LUMO leads to partial charge transfer between metal and molecular layer, shifting HOMO or LUMO closer to the Fermi level, creating a new dipole whose strength and direction depend on the former initial levels. [45–47]. This has been investigated with density functional theory calculations in the case on various molecules chemisorbed on gold, with different tail groups [48–52]. In the case of aromatic SAMs, the position of the HOMO is found to be independent on the tail group, in the range -0.98 to -1.1 eV below the Fermi level, whereas the LUMO position varies with the tail group function, shifting the WF in the same direction [48,49]. The calculations show indeed two dominant contributions to the WF value, the bond dipole and the tail dipole. The others dipoles along the molecule contribute less, screened by the dielectric character of densely packed layer.[53,54] The Au-S bond dipole reduces the work function by ~ 1.2 eV compared to a clean Au surface, and is similar for numerous SAM of alkyl or aromatic thiols [48,53]. The main source of WF differences between different aromatic SAMs depend on the tail function. An electron donor function (respectively electron acceptor) leads to a reduction (increase) of the work function[48,54].

We can then discuss the change we observed taking into account these considerations. A consequence of the irradiation induced cross linking is the chemical

disorder in the layer [40,42–44] because molecules need to twist and bend toward neighboring molecules for the creation of new bonds. The cross section for chemical disorder and WF reduction are in the same order of magnitude. In addition, Fig. 2.c shows that domain boundaries, which are regions of disorder, both in pristine and irradiated areas have lower WF than long range ordered domains. This observation points to increased disorder as a reason for WF change, but the comparison has to be taken with care because boundaries are often associated with vacancies [55,56], whereas it has been showed by following XPS C1s signature XPS that irradiation only marginally affect the overall molecular density [39,57]. In other words, the disorder induced by irradiation doesn't mimic the disorder at the domain boundaries. Moreover, the boundaries also suffer a WF reduction, showing that changes can affect both ordered and disordered regions. Chemical disorder consists also of the alteration of the Au-S bonds, and formation of R-SS-R or R-S-R function, visible in XPS S 2p signatures [39,40,43,44]. The estimated cross section for this alteration is $0.5 - 1.5 \times 10^{-17} \text{ cm}^2$, in the range, or slightly lower than WF change cross section ($1.6 \times 10^{-17} \text{ cm}^2$). To our knowledge, there is no mention in the calculations of such anchoring group alteration effects on the WF in literature, although it can take part in the WF change. The contribution of formation of the new CC bonds that cross link adjacent molecules must also be considered. The hybridization of the carbon centers is overall unchanged in HREELS signature after irradiation at 50 eV. This is consistent with NEXAFS observations of irradiated aromatic SAMS [40,58], and with the observation to a reduced gap between HOMO and LUMO [59], associated to the extension of π molecular orbitals. Due to Fermi level pinning of the HOMO, this gap reduction shifts the LUMO to lower energy, reducing the work function. The hydrogen loss is also expected to create radicals, leaving the C atom with an unpaired electron, with a twofold consequence in WF reduction. Firstly, the system gain an electron donating character, which is associated to low WF [48]. Secondly, when created on the tail C-H function, this radical has an extended lifetime in high vacuum, which then leads to a decrease of the small but existing dipole along the C-H function. This contribution to the WF reduction must be considered, as the cross section measured from C-H content loss HREELS ($2.7-4.7 \times 10^{-17} \text{ cm}^2$) and WF reduction cross section are compatible. The tail dipole is also the main source of differences between different thiol aromatic SAMS on gold, so affecting the tail dipole is expected to have consequences on the

WF. It can also explain why the WF slightly increases with the aging of the irradiated layer. The point is discussed in the next paragraph.

Stability issue – H content sensitivity to environment

The hydrogen content of an irradiated, in other words damaged, molecular film is very sensitive to its history and environment. Actually, such a film presents a moderate stability when exposed either to residual vacuum for a long time or to air during transfer. Pristine TPT SAMs were processed using low-energy electrons as described above, and then left for one night under ultra-high vacuum. The evolution of the chemical composition of the molecular layer was followed *in situ* by HREELS, as shown in Fig. 5. The stretching CH_x bands of the TPT SAM before and after irradiation at 50 eV were already described above: the band is not modified in shape, but its intensity decreases strongly. This was interpreted as resulting from a strong decrease of the hydrogen content of the film without noticeable change of hybridization of the remaining hydrogenated carbon centres. After an exposure to the residual atmosphere of the ultra-high vacuum chamber for about twelve hours, the band shape and intensity change. The contribution of $\nu(\text{sp}^3\text{-CH}_x)$ modes increases, while the structure attributed to $\nu(\text{sp}^2\text{-CH}_x)$ modes remain unchanged. Additional hydrogen atoms were incorporated into the processed layer after one night exposure to residual vacuum, in the form of saturated hydrogenated carbon centres. This can be interpreted as follows. The unstable radical centres left onto the sample (sub-)surface after irradiation get hydrogen saturated by extended exposure to the residual atmosphere of the UHV chamber. This observation is important because experiments made with different pressure conditions may have alternative results, as radical stability is reduced in higher pressure. This is probably why the measurements by Kelvin probe microscopy may exhibit different behaviour with the WF changed induced by irradiation. Yildirim et al. [60] measured a WF increase from 4.35 eV to 4.55 eV with 50 eV irradiation made under 10^{-8} mbar of H_2 pressure.

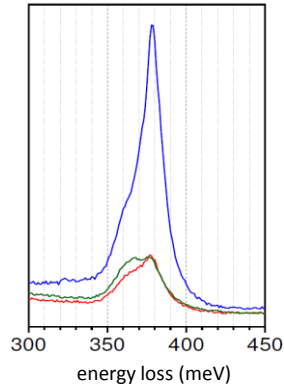


Figure 5: $\nu(sp^m-CH_x)$ band probed using vibrational spectroscopy ($E_{HREELS} = 6$ eV, resolution $\Delta E_{FWHM} = 6-8$ meV). Chemical modification of fresh TPT SAM (blue curve) submitted to electron irradiation at 50 eV (dose: 9.5 mC.cm⁻², red curve) and then exposed to residual UHV vacuum overnight (green curve).

In order to get complementary data onto the electronic structure of the LEE processed TPT layers, the samples were air-transferred to another experimental setup, equipped with Photoemission Electron Microscopy (PEEM). The same trend of variation is observed as a function of the irradiation energy, but the observed decreases are more than twice smaller. This confirms the relation between the hydrogen content of the film and the reduction of its work function.

The absolute WF values of the irradiated spots in TPT SAMs were measured by PEEM with a He-I (21.2 eV) source at the photoemission threshold. A typical PEEM image (Fig. 6(a)) recorded at a kinetic energy of 4.45 eV shows that the irradiated areas have higher emitted intensity compared to the unirradiated areas. The kinetic energy scale is calibrated with respect to the Fermi level of the metallic sample holder, itself in electrical contact with the sample. The threshold value is therefore the sample WF. The local threshold spectra (Fig. 6(b)) shows that the Fermi level is from 4.2 to 4.5 eV lower with respect to the vacuum level, which is 0.6-0.8 eV lower than the calculated values in ref.[49]. The local threshold spectra (Fig. 6(b)) indicate the WF variance after electron irradiation with energies from 10 eV to 50 eV. The WF values obtained by error function fitting to the corresponding curves in Fig. 6(b) are plotted in Fig. 6(c) as a function of the irradiation energy. In comparison with the LEEM results (Fig. 3), they show the same trend of WF change when irradiation energy increases from 10 to 50

eV. However, in LEEM, the maximum WF difference is ~ 0.27 eV compared to only ~ 0.09 eV in PEEM. The exposure of the irradiated TPT SAMs to atmosphere, which brings possible TPT film degradation and contamination, may attenuate the irradiation induced difference in WF between LEEM and PEEM measurements. This indicates that the contribution of the radicals in the WF decrease is important, as these radicals are susceptible to react during exposure to air, especially those at the tail CH bond. The slight rise of WF in the 50 eV irradiated area with respect to that in the 40 eV irradiated area is notable in both LEEM (Fig. 3(d)) and PEEM (Fig. 6(c)). It implies that the chemical modification induced by irradiation varies in the energy range of 40 to 50 eV. We suspect that the primary mechanism starting the chemistry under electron impact has a key role: among the different processes able to start chemical reaction by irradiation induced bond cleavage, electron impact ionization is believed to be dominant at 50 eV [31] whereas dissociative electronic excitation and dissociative electronic attachment dominate at lower energy [61,62].

Among the three parameters discussed earlier, we have access to evidence of Fermi level pinning through the PEEM spectra of the irradiated regions. The PEEM spectra at high kinetic energy in the valence band maximum (VBM) region shown in Fig. 4(d) taken in the same sample location give information on the HOMO positions of our TPT SAMs under above mentioned irradiation at different energies. We calculated that the ionization potential (IP) of TPT is about 7.2 eV [35], Wang et al.[51] found that the IP of a biphenylthiol backbone is 7.61 eV, i.e. the HOMO is located about 7.2-7.6 eV lower than the vacuum level. This rough estimation is more accurate in ref. [49] where the IP of a TPT SAM is 4.65 eV including the corrections from the layer organisation and the bond dipole formation. It gives the HOMO position 0.98 eV below the Fermi level, with a calculated WF of 3.66 eV. Near the Fermi edge of the photoemission spectra, two structures can be identified at 19.2 eV and 18.6 eV (figure 4d). Considering the photon energy of our He-I source for PEEM is 21.2 eV, 19.2 eV gives a HOMO position at $E-E_F=19.2 - 21.2 = -2$ eV. This is 1 eV below the calculated values. Feng et co-workers [59] measured by UPS a HOMO position 3.6 eV below the Fermi level for terphenyl-dimethanethiol, with a HOMO very similar associated to the aromatic backbone of the molecule. They observed also that the HOMO position in aromatic SAMs on Au does not shift with respect to the Fermi level following irradiations. The peaks we observed persist in the same energy position under irradiations at the different energies used in this work. This confirms the fermi-level pinning of the HOMO, in agreement with ref [59]

which indicates that the WF reduction is due to lowering of the LUMO level and irradiation induced changes in the tail-group.

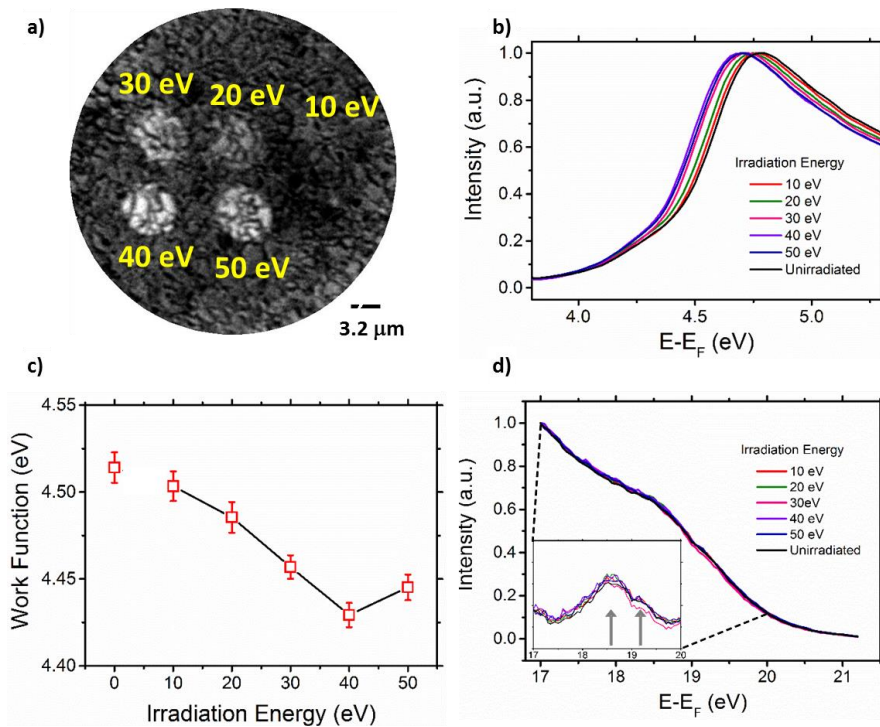


Figure 5: (a) He-I (21.2 eV) PEEM image of areas irradiated with different energies (indicated in the image) taken at electron energy 0.45 eV with respect to fermi level. (b) Local threshold spectra for areas irradiated with different energies. (c) Work function values extracted from (b). (d) PEEM spectra at high energy cut-off.

Conclusion

We use a LEEM to perform well defined microscopic electron irradiation with given energy and estimated dose. The irradiated area can be precisely confined to micrometre size as the illuminating electron beam is selected by an aperture. WF decrease in TPT SAMs anchored on Au substrate induced by low energy (up to 50 eV)

electron irradiation is observed by LEEM and PEEM. Such WF decrease is correlated with both irradiation energy and dose. The maximum WF decrease is about 0.27 eV, obtained from 40 eV irradiation for 5 min. The WF decrease can be interpreted as a consequence of the loss of hydrogen and subsequent new bond formation, radical creation, and increase of disorder, including Au-S bond alteration. The map of WF change showing the extent of WF decrease for organized domains and their boundaries confirms that disorder is not the only source of WF decrease. By comparing the cross-sections of the different processes, we conclude that the alteration of the Au-S bond may be involved in the WF decrease, but its efficiency cannot render the measured efficiency of the overall process. In agreement with studies reported in the literature, we also observed that the HOMO remains pinned to the Fermi-level after irradiation, showing that the charge transfer to gold is able to stabilize the radicals or the new orbitals formed after hydrogen desorption. As a consequence, a lowering of the LUMO, as reported also in literature, can also contribute to WF reduction. The radical can be located at the tail, where it may affect the tail dipole which is a major source of WF difference in aromatic SAMs theoretical investigations gathered in the literature. The cross section of H loss is compatible with the dynamic observed for the measured WF decrease.

Experimental

Gold substrates. Glass substrates (11×11 mm) coated successively with a 2.5 nm adhesion layer of chromium and a 250 nm thick layer of gold were purchased from Arrandee (Werther, Germany). The gold-coated substrates were flame-annealed to ensure good crystallinity of the (111) textured, topmost layers with micrometre to submicrometre domains [15,32,33]. The surfaces of the substrates were examined by an atomic force microscope (AFM) in atmosphere. Lattice orientation at different areas of the Au layers was checked using the diffraction imaging mode of the LEEM, also

called μ -LEED (low energy electron diffraction) and combined with an aperture to confine the beam diameter to about 2 μm to produce well-defined diffraction patterns.

SAMs. The substrates were immersed in freshly prepared saturated solutions of thiol in absolute ethanol at a dilution of ~ 1 mM for 2 h under stirring, following a procedure applied to a series of thiol SAMs [31,63,64]. After 5 min of sonication and rinsing in ethanol (15 min) to evacuate all non-covalently bound molecules, the surfaces were rinsed in Milli-Q water for 15 min and then dried under a flow of dry nitrogen. The presence of a layer of TPT in the standing-up phase was checked by X-ray photoemission spectroscopy (XPS), after transferring the sample from one experiment to the other, and the thickness was estimated to be ~ 15 Å [65]. For the chemical characterization of the molecular layers, we used High Resolution Electron Energy Loss Spectroscopy (HREELS), model IB500 Omicron. Vibrational energy loss spectra were measured at room temperature, in the specular geometry ($\theta_i = \theta_r = 55^\circ$ with respect to the normal to the sample surface), and with an incident probing current of 30 pA. The probing energy was set at $E_{\text{HREELS}} = 6$ eV, with a resolution of ~ 6 -8 meV taken as the full width at half maximum (FWHM) of the elastic peak. The well-isolated CH stretching band is a good indicator for quality of the prepared TPT SAMs. The band is intense, well isolated, located at 378 meV, and results from the overlapping contributions of the unresolved stretching modes $\nu(\text{sp}^2\text{-CH})$ (see Fig. 4). The shoulder visible at 364 meV can be attributed to partial carbon rehybridization, associated with a reduced number of flat-lying molecules [66], although a combination of losses from lower energy modes and partial solvent pollution cannot be completely excluded.

Low energy electron irradiations of the TPT SAMs and the main characterizations were performed using an Elmitec LEEM III [19] equipped with an energy analyzer. The SAM samples were located in the main ultrahigh vacuum (UHV) chamber with a base pressure of 3×10^{-10} mbar during the experiments. The e-beam for imaging and irradiation was produced through a Schottky field electron gun in LEEM, then was aligned and focused by a series of illumination optics before reaching the sample. The imaging and irradiation of the samples were carried out at room temperature using the same illumination system, only changing the electron energy. An aperture with a diameter of 100 μm was used to give an incident beam spot of about 5 μm diameter in slightly elliptical shape on the sample surface. Unfortunately, we are not able to carry out precise current measurement of the irradiating e-beam in our LEEM apparatus. An

estimation of the irradiation dose is done here in light of a recent work using the same apparatus [67]. A gun emission current of 20 nA provides a 90 μm e-beam collimated to 5 μm by a diaphragm. Therefore, the irradiation dose for a 1 min exposure is about 19 $\text{mC}\cdot\text{cm}^2$. Two series of irradiations were performed at different sample positions, one is with incremental incident energy from 10 to 50 eV for fixed exposure time of 5 min and the other is with incremental exposure time from 1 to 30 min at fixed incident energies of 10 eV and 50 eV. Between irradiations the beam shutter was closed while moving the sample to a fresh area. All the irradiations were performed in the same 40 μm field view, i.e. the same magnification and the same incident electron flux density.

The WF is obtained by measuring the transition from mirror electron microscopy (MEM) mode to LEEM imaging mode [36,37] immediately after each irradiation. The transition from MEM to LEEM is identifiable by a sharp fall of electron reflectivity as the incident electron energy, also called the start voltage, is increased. The image series include all the irradiated area. By extracting the MEM to LEEM transition intensity curves for areas with different irradiating conditions and fitting with error function [38], we determine the positions of the MEM-LEEM transition, i.e. the WF of the irradiated regions.

After LEEM measurements, the irradiated sample was stored in the UHV chamber of LEEM for seven days at 10^{-10} mbar and exposed to air for two hours during transfer into the energy-filtered PEEM (ScientaOmicron) for imaging with highly focused He-I (21.2 eV) source. With a pass energy of 50 eV and an energy slit width of 1.0 mm, an energy resolution of about 0.2 eV is achieved in our spectromicroscope. The WF values of TPT film with different irradiation energies from 10 eV to 50 eV are measured with local threshold spectra extracted from image sequence taken with an energy step of 0.025 eV. The HOMO of the TPT film with different irradiation conditions were studied in the PEEM spectra at higher kinetic energy near the valence band maximum (VBM).

Acknowledgements

The authors thank Dr. Justine Houplin for her contribution to the first observation of the effect on TPT SAM of an overnight exposure to residual vacuum. The authors thank Dr. Elizabeth Boer-Duchemin and Dr. Céline Dablemont from the ISMO for helping them with SAMs preparation and giving them access to an AFM. This work has received funding from the international ANR-DFG program HREELM (ANR-14-CE35-0019). It was also supported by the European Union's Horizon 2020 research and innovation program under the Marie Skłodowska-Curie grant agreement No 722149 (ELENA Innovative Training Network, Low energy ELEctron driven chemistry for the advantage of emerging Nano-fabrication methods). This work has received funding from "Investissements d'Avenir" program from PALM LabEx (ANR-10-LABX-0039-PALM).

References

- [1] Park, J.; Sempionatto, J.R.; Kim, J.; Jeong, Y.; Gu, J.; Wang, J.; Park, I. Microscale Biosensor Array Based on Flexible Polymeric Platform toward Lab-on-a-Needle: Real-Time Multiparameter Biomedical Assays on Curved Needle Surfaces. *ACS Sens.*, **2020**, *5*, 1363–1373.
- [2] Kherbouche, I.; Luo, Y.; Félidj, N.; Mangeney, C. Plasmon-Mediated Surface Functionalization: New Horizons for the Control of Surface Chemistry on the Nanoscale. *Chem. Mater.*, **2020**, *32*, 5442–5454.
- [3] Hong, T.; Liu, W.; Li, M.; Chen, C. Click Chemistry at the Microscale. *The Analyst*, **2019**, *144*, 1492–1512.
- [4] Hunt, H.K.; Armani, A.M. Label-Free Biological and Chemical Sensors. *Nanoscale*, **2010**, *2*, 1544.
- [5] Sajfutdinow, M.; Uhlig, K.; Prager, A.; Schneider, C.; Abel, B.; Smith, D.M. Nanoscale Patterning of Self-Assembled Monolayer (SAM)-Functionalised Substrates with Single Molecule Contact Printing. *Nanoscale*, **2017**, *9*, 15098–15106.
- [6] Xu, S.; Miller, S.; Laibinis, P.E.; Liu, G. Fabrication of Nanometer Scale Patterns within Self-Assembled Monolayers by Nanografting. *Langmuir*, **1999**, *15*, 7244–7251.
- [7] Götzhäuser, A.; Geyer, W.; Stadler, V.; Eck, W.; Grunze, M.; Edinger, K.; Weimann, T.; Hinze, P. Nanoscale Patterning of Self-Assembled Monolayers with Electrons. *J. Vac. Sci. Technol. B*, **2000**, *18*, 3414–3418.
- [8] Turchanin, A.; Tinazli, A.; El-Desawy, M.; Großmann, H.; Schnietz, M.; Solak, H.H.; Tampé, R.; Götzhäuser, A. Molecular Self-Assembly, Chemical Lithography, and

- Biochemical Tweezers: A Path for the Fabrication of Functional Nanometer-Scale Protein Arrays. *Adv. Mater.*, **2008**, *20*, 471–477.
- [9] Humblot, V.; Yala, J.-F.; Thebault, P.; Boukerma, K.; Héquet, A.; Berjeaud, J.-M.; Pradier, C.-M. The Antibacterial Activity of Magainin I Immobilized onto Mixed Thiols Self-Assembled Monolayers. *Biomaterials*, **2009**, *30*, 3503–3512.
- [10] Valotteau, C.; Calers, C.; Casale, S.; Berton, J.; Stevens, C.V.; Babonneau, F.; Pradier, C.-M.; Humblot, V.; Baccile, N. Biocidal Properties of a Glycosylated Surface: Sphorolipids on Au(111). *ACS Appl. Mater. Interfaces*, **2015**, *7*, 18086–18095.
- [11] Bald, I.; Langer, J.; Tegeder, P.; Ingólfsson, O. From Isolated Molecules through Clusters and Condensates to the Building Blocks of Life. *Int. J. Mass Spectrom.*, **2008**, *277*, 4–25.
- [12] Arumainayagam, C.R.; Lee, H.-L.; Nelson, R.B.; Haines, D.R.; Gunawardane, R.P. Low-Energy Electron-Induced Reactions in Condensed Matter. *Surf. Sci. Rep.*, **2010**, *65*, 1–44.
- [13] Lafosse A.; Azria R. Chap. 7. In *Low-Energy Electron Scattering from Molecules, Biomolecules and Surfaces*; CRC Press Taylor & Francis Group, **2012**.
- [14] Schreiber, F. Self-Assembled Monolayers: From Simple Model Systems to Biofunctionalized Interfaces. *J. Phys. Condens. Matter*, **2004**, *16*, R881–R900.
- [15] Love, J.C.; Estroff, L.A.; Kriebel, J.K.; Nuzzo, R.G.; Whitesides, G.M. Self-Assembled Monolayers of Thiolates on Metals as a Form of Nanotechnology. *Chem. Rev.*, **2005**, *105*, 1103–1170.
- [16] Turchanin, A.; Götzhäuser, A. Carbon Nanomembranes from Self-Assembled Monolayers: Functional Surfaces without Bulk. *Prog. Surf. Sci.*, **2012**, *87*, 108–162.
- [17] Götzhäuser, A.; Geyer, W.; Stadler, V.; Eck, W.; Grunze, M.; Edinger, K.; Weimann, Th.; Hinze, P. Nanoscale Patterning of Self-Assembled Monolayers with Electrons. *J. Vac. Sci. Technol. B Microelectron. Nanometer Struct.*, **2000**, *18*, 3414.
- [18] Küller, A.; Eck, W.; Stadler, V.; Geyer, W.; Götzhäuser, A. Nanostructuring of Silicon by Electron-Beam Lithography of Self-Assembled Hydroxybiphenyl Monolayers. *Appl. Phys. Lett.*, **2003**, *82*, 3776–3778.
- [19] Altman, M.S. Trends in Low Energy Electron Microscopy. *J. Phys. Condens. Matter*, **2010**, *22*, 084017.
- [20] Houplin, J.; Amiaud, L.; Dablemont, C.; Lafosse, A. DOS and Electron Attachment Effects in the Electron-Induced Vibrational Excitation of Terphenylthiol SAMs. *Phys. Chem. Chem. Phys.*, **2015**, *17*, 30721–30728.
- [21] Tai, Y.; Shaporenko, A.; Noda, H.; Grunze, M.; Zharnikov, M. Fabrication of Stable Metal Films on the Surface of Self-Assembled Monolayers. *Adv. Mater.*, **2005**, *17*, 1745–1749.
- [22] Ballav, N.; Schilp, S.; Zharnikov, M. Electron-Beam Chemical Lithography with Aliphatic Self-Assembled Monolayers. *Angew. Chem. Int. Ed.*, **2008**, *47*, 1421–1424.
- [23] Schreiber, F. Structure and Growth of Self-Assembling Monolayers. *Prog. Surf. Sci.*, **2000**, *65*, 151–256.
- [24] Frey, S.; Stadler, V.; Heister, K.; Eck, W.; Zharnikov, M.; Grunze, M.; Zeysing, B.; Terfort, A. Structure of Thioaromatic Self-Assembled Monolayers on Gold and Silver. *Langmuir*, **2001**, *17*, 2408–2415.
- [25] Amiaud, L.; Houplin, J.; Bourdier, M.; Humblot, V.; Azria, R.; Pradier, C.-M.; Lafosse, A. Low-Energy Electron Induced Resonant Loss of Aromaticity: Consequences on Cross-Linking in Terphenylthiol SAMs. *Phys. Chem. Chem. Phys.*, **2014**, *16*, 1050–1059.
- [26] Tanuma, S.; Powell, C.J.; Penn, D.R. Calculations of Electron Inelastic Mean Free Paths. *Surf Interface Anal.*, **1993**, *21*, 165–176.

- [27] Seah, M.P.; Dench, W.A. Quantitative Electron Spectroscopy of Surfaces: A Standard Data Base for Electron Inelastic Mean Free Paths in Solids. *Surf. Interface Anal.*, **1979**, *1*, 2–11.
- [28] Goulet, T. Low-Energy (0-10 eV) Electron Transmission through Solid Thin Benzene Films. 5.
- [29] Houdoux, D.; Houplin, J.; Amiaud, L.; Lafosse, A.; Dablemont, C. Interfacial Water on Organic Substrates at Cryogenic Temperatures: Hydrogen Bonding and Quantification in the Submonolayer Regime. *Phys Chem Chem Phys*, **2017**, *19*, 2304–2312.
- [30] Pireaux, J.J.; Gregoire, C.; Caudano, R.; Vilar, M.Rei.; Brinkhuis, R.; Schouten, A.J. Electron-Induced Vibrational Spectroscopy. A New and Unique Tool to Unravel the Molecular Structure of Polymer Surfaces. *Langmuir*, **1991**, *7*, 2433–2437.
- [31] Houplin, J.; Dablemont, C.; Sala, L.; Lafosse, A.; Amiaud, L. Electron Processing at 50 eV of Terphenylthiol Self-Assembled Monolayers: Contributions of Primary and Secondary Electrons. *Langmuir*, **2015**, *31*, 13528–13534.
- [32] Dishner, M.H.; Ivey, M.M.; Gorer, S.; Hemminger, J.C.; Feher, F.J. Preparation of Gold Thin Films by Epitaxial Growth on Mica and the Effect of Flame Annealing. *J. Vac. Sci. Technol. A*, **1998**, *16*, 3295–3300.
- [33] Arrandee metal GmbH; <http://www.arrandee.com/>. Arrandee, Usage. [Http://www.Arrandee.Com/](http://www.arrandee.com/).
- [34] Amiaud, L.; Houplin, J.; Bourdier, M.; Humblot, V.; Azria, R.; Pradier, C.-M.; Lafosse, A. Low-Energy Electron Induced Resonant Loss of Aromaticity: Consequences on Cross-Linking in Terphenylthiol SAMs. *Phys Chem Chem Phys*, **2014**, *16*, 1050–1059.
- [35] Houplin, J.; Amiaud, L.; Sedzik, T.; Dablemont, C.; Teillet-Billy, D.; Rougeau, N.; Lafosse, A. A Combined DFT/HREELS Study of the Vibrational Modes of Terphenylthiol SAMs. *Eur. Phys. J. D*, **2015**, *69*.
- [36] Murata, Y.; Starodub, E.; Kappes, B.B.; Ciobanu, C.V.; Bartelt, N.C.; McCarty, K.F.; Kodambaka, S. Orientation-Dependent Work Function of Graphene on Pd(111). *Appl. Phys. Lett.*, **2010**, *97*, 143114.
- [37] Barrett, N.; Rault, J.E.; Wang, J.L.; Mathieu, C.; Locatelli, A.; Mentès, T.O.; Nino, M.A.; Fusil, S.; Bibes, M.; Barthelemy, A.; Sando, D.; Ren, W.; Prosandeev, S.; Bellaïche, L.; Vilquin, B.; Petraru, A.; Krug, I.P.; Schneider, C.M. Full Field Electron Spectromicroscopy Applied to Ferroelectric Materials. *J. Appl. Phys.*, **2013**, *113*, 187217.
- [38] Renault, O.; Brochier, R.; Roule, A.; Haumesser, P.-H.; Krömker, B.; Funnemann, D. Work-Function Imaging of Oriented Copper Grains by Photoemission. *Surf. Interface Anal.*, *38*, 375–377.
- [39] Angelova, P.; Vieker, H.; Weber, N.-E.; Matei, D.; Reimer, O.; Meier, I.; Kurasch, S.; Biskupek, J.; Lorbach, D.; Wunderlich, K.; Chen, L.; Terfort, A.; Klapper, M.; Müllen, K.; Kaiser, U.; Götzhäuser, A.; Turchanin, A. A Universal Scheme to Convert Aromatic Molecular Monolayers into Functional Carbon Nanomembranes. *ACS Nano*, **2013**, *7*, 6489–6497.
- [40] Weidner, T.; Ballav, N.; Grunze, M.; Terfort, A.; Zharnikov, M. Modification of Biphenylselenolate Monolayers by Low-Energy Electrons. *Phys. Status Solidi B*, **2009**, *246*, 1519–1528.
- [41] Geyer, W.; Stadler, V.; Eck, W.; Zharnikov, M.; Götzhäuser, A.; Grunze, M. Electron-Induced Crosslinking of Aromatic Self-Assembled Monolayers: Negative Resists for Nanolithography. *Appl. Phys. Lett.*, **1999**, *75*, 2401–2403.
- [42] Zharnikov, M.; Grunze, M. Modification of Thiol-Derived Self-Assembling Monolayers by Electron and x-Ray Irradiation: Scientific and Lithographic Aspects. *J. Vac. Sci. Technol. B*, **2002**, *20*, 1793–1807.

- [43] Meyerbroeker, N.; Waske, P.; Zharnikov, M. Amino-Terminated Biphenylthiol Self-Assembled Monolayers as Highly Reactive Molecular Templates. *J. Chem. Phys.*, **2015**, *142*, 101919.
- [44] Koch, S.; Kaiser, C.D.; Penner, P.; Barclay, M.; Frommeyer, L.; Emmrich, D.; Stohmann, P.; Abu-Husein, T.; Terfort, A.; Fairbrother, D.H.; Ingólfsson, O.; Götzhäuser, A. Amplified Cross-Linking Efficiency of Self-Assembled Monolayers through Targeted Dissociative Electron Attachment for the Production of Carbon Nanomembranes. *Beilstein J. Nanotechnol.*, **2017**, *8*, 2562–2571.
- [45] Ishii, H.; Sugiyama, K.; Ito, E.; Seki, K. Energy Level Alignment and Interfacial Electronic Structures at Organic/Metal and Organic/Organic Interfaces. *Adv. Mater.*, **1999**, *11*, 605–625.
- [46] Kahn, A. Fermi Level, Work Function and Vacuum Level. *Mater. Horiz.*, **2016**, *3*, 7–10.
- [47] Kahn, A.; Koch, N.; Gao, W. Electronic Structure and Electrical Properties of Interfaces between Metals and π -Conjugated Molecular Films. *J. Polym. Sci. Part B Polym. Phys.*, **2003**, *41*, 2529–2548.
- [48] Heimel, G.; Romaner, L.; Brédas, J.-L.; Zojer, E. Interface Energetics and Level Alignment at Covalent Metal-Molecule Junctions: π -Conjugated Thiols on Gold. *Phys. Rev. Lett.*, **2006**, *96*.
- [49] Heimel, G.; Romaner, L.; Zojer, E.; Brédas, J.-L. Toward Control of the Metal–Organic Interfacial Electronic Structure in Molecular Electronics: A First-Principles Study on Self-Assembled Monolayers of π -Conjugated Molecules on Noble Metals. *Nano Lett.*, **2007**, *7*, 932–940.
- [50] Heimel, G.; Romaner, L.; Brédas, J.-L.; Zojer, E. Organic/Metal Interfaces in Self-Assembled Monolayers of Conjugated Thiols: A First-Principles Benchmark Study. *Surf. Sci.*, **2006**, *600*, 4548–4562.
- [51] Wang, L.; Rangger, G.M.; Romaner, L.; Heimel, G.; BucìEko, T.; Ma, Z.; Li, Q.; Shuai, Z.; Zojer, E. Electronic Structure of Self-Assembled Monolayers on Au(111) Surfaces: The Impact of Backbone Polarizability. *Adv. Funct. Mater.*, **2009**, *19*, 3766–3775.
- [52] Rusu, P.C.; Brocks, G. Work Functions of Self-Assembled Monolayers on Metal Surfaces by First-Principles Calculations. *Phys. Rev. B*, **2006**, *74*.
- [53] Deutsch, D.; Natan, A.; Shapira, Y.; Kronik, L. Electrostatic Properties of Adsorbed Polar Molecules: Opposite Behavior of a Single Molecule and a Molecular Monolayer. *J. Am. Chem. Soc.*, **2007**, *129*, 2989–2997.
- [54] Heimel, G.; Romaner, L.; Zojer, E.; Bredas, J.-L. The Interface Energetics of Self-Assembled Monolayers on Metals. *Acc. Chem. Res.*, **2008**, *41*, 721–729.
- [55] Yang, G.; Liu, G. New Insights for Self-Assembled Monolayers of Organothiols on Au(111) Revealed by Scanning Tunneling Microscopy. *J. Phys. Chem. B*, **2003**, *107*, 8746–8759.
- [56] Poirier, G.E. Characterization of Organosulfur Molecular Monolayers on Au(111) Using Scanning Tunneling Microscopy. *Chem. Rev.*, **1997**, *97*, 1117–1128.
- [57] Yildirim, C.; Füser, M.; Terfort, A.; Zharnikov, M. Modification of Aromatic Self-Assembled Monolayers by Electron Irradiation: Basic Processes and Related Applications. *J. Phys. Chem. C*, **2017**, *121*, 567–576.
- [58] Frey, S.; Rong, H.-T.; Heister, K.; Yang, Y.-J.; Buck, M.; Zharnikov, M. Response of Biphenyl-Substituted Alkanethiol Self-Assembled Monolayers to Electron Irradiation: Damage Suppression and Odd–Even Effects. *Langmuir*, **2002**, *18*, 3142–3150.
- [59] Feng, D.-Q.; Wisbey, D.; Losovyj, Ya.B.; Tai, Y.; Zharnikov, M.; Dowben, P.A. Electronic Structure and Polymerization of a Self-Assembled Monolayer with Multiple Arene Rings. *Phys. Rev. B*, **2006**, *74*.

- [60] Yildirim, C.; Sauter, E.; Terfort, A.; Zharnikov, M. Effect of Electron Irradiation on Electric Transport Properties of Aromatic Self-Assembled Monolayers. *J. Phys. Chem. C*, **2017**, *121*, 7355–7364.
- [61] Arumainayagam, C.R.; Lee, H.-L.; Nelson, R.B.; Haines, D.R.; Gunawardane, R.P. Low-Energy Electron-Induced Reactions in Condensed Matter. *Surf. Sci. Rep.*, **2010**, *65*, 1–44.
- [62] Böhrer, E.; Warneke, J.; Swiderek, P. Control of Chemical Reactions and Synthesis by Low-Energy Electrons. *Chem. Soc. Rev.*, **2013**, *42*, 9219.
- [63] Briand, E.; Salmain, M.; Herry, J.-M.; Perrot, H.; Compère, C.; Pradier, C.-M. Building of an Immunosensor: How Can the Composition and Structure of the Thiol Attachment Layer Affect the Immunosensor Efficiency? *Biosens. Bioelectron.*, **2006**, *22*, 440–448.
- [64] Tielens, F.; Costa, D.; Humblot, V.; Pradier, C.-M. Characterization of ω -Functionalized Undecanethiol Mixed Self-Assembled Monolayers on Au(111): A Combined Polarization Modulation Infrared Reflection–Absorption Spectroscopy/X-Ray Photoelectron Spectroscopy/Periodic Density Functional Theory Study. *J. Phys. Chem. C*, **2008**, *112*, 182–190.
- [65] *Arrandee Metal GmbH*. [Http://Www.Arrandee.Com/](http://www.rrandee.com/).
- [66] Rufael, T.S.; Huntley, D.R.; Mullins, D.R.; Gland, J.L. Adsorption and Reactions of Benzenethiol on the Ni(111) Surface. *J. Phys. Chem.*, **1994**, *98*, 13022–13027.
- [67] Nataf, G.F.; Guennou, M.; Kreisel, J.; Hicher, P.; Haumont, R.; Aktas, O.; Salje, E.K.H.; Tortech, L.; Mathieu, C.; Martinotti, D.; Barrett, N. Control of Surface Potential at Polar Domain Walls in a Nonpolar Oxide. *Phys. Rev. Mater.*, **2017**, *1*, 074410.